

Fast single pixel modal wavefront sensing using neural networks

ANTONY ORTH^{1*}, OLIVER PITTS¹, COSTEL FLUERARU¹, TERRENCE STEWART¹, HAMED AKHLAGHI², MOHAMADREZA PASHAZANOOSI², MICHAEL TAYLOR², STEVE HRANILOVIC²

¹*National Research Council Canada, Ottawa, Ontario, Canada*

²*Department of Electrical and Computer Engineering, McMaster University, Hamilton, Ontario, Canada*

**anton.y.orth@nrc-cnrc.gc.ca*

Abstract: Dynamic wavefront aberrations negatively impact a wide range of optical applications including astronomy, optical free-space telecommunications and bio-imaging. Wavefront errors can be compensated by an adaptive optics system comprised of a deformable mirror and wavefront sensor connected by a control loop. For satellite optical communications (SatCom), wavefront sensing is particularly challenging due to the rapid wavefront fluctuations induced by strong turbulence and movement of the transmitting satellite across the sky. Existing wavefront sensing techniques require fast cameras ($>1\text{kHz}$) that are not widely available at wavelengths suitable for SatCom (e.g., 1550nm and mid-to-long wave infrared). Here, we propose a new wavefront sensing technique that uses a single photodiode and a fast mirror to make phase-diverse intensity measurements of the incoming wavefront. We train neural networks to accurately estimate the input phase given this phase-diverse sub-millisecond intensity trace. Our simulations show that our technique is robust in cases of strong turbulence where previous modal wavefront sensors fail due to modal crosstalk, achieving 99% of the optimal Strehl ratio from a 50-mode correction at a sensing rate of 2kHz. We explore typical cases of turbulence magnitude, sensing speed and noise that might be encountered by such a system.

1. Introduction

Aberrated wavefronts occur in many optical applications, from imaging in biological tissue to optical astronomy and free space optical communication. These aberrations have a significant negative impact and must be corrected to approach optimal system performance. Adaptive optics (AO) approaches are widely exploited to perform these corrections. A typical AO system consists of a combination of a wavefront sensor (WFS) to measure the aberration and a tunable phase delay element, such as a deformable mirror (DM), to perform the correction. The DM is actuated such that it imparts the opposite of the aberration measured by the WFS onto the incoming aberrated beam. The outgoing beam is therefore phase-corrected to the extent possible using the finite degrees of freedom of the DM. The quality of the phase correction is further impacted by the accuracy of the wavefront sensor and the temporal bandwidth of the aberrations.

In this work we consider the impact of the turbulent atmosphere on a propagating laser beam for optical communications. In optical satellite communications (optical SatCom), a laser beam passes through the turbulent atmosphere, subjecting it to severe phase distortions that fluctuate rapidly in time. The strength of the phase distortions is often described by ratio of the receiver aperture D to the Fried parameter r_0 , which describes the transverse correlation length of the phase distortion. For $\frac{D}{r_0} < 1$ turbulence has little effect on incoming wavefront, while for $\frac{D}{r_0} > 10$, as are routinely encountered in optical SatCom [1–3], the incoming wavefront is severely distorted. At the receiver aperture, the beam must be focused down for injection into a single

mode optical fiber to enter a fiber-based communication network. If the incoming wavefront carries phase distortion (i.e., is not flat), the focused beam resembles a dynamic speckle pattern that does not couple efficiently into a single mode fiber. This causes a severe loss of signal coupled into the communication channel, restricting or halting data throughput altogether. Efficient and accurate AO at the receiver is therefore a crucial component for any high-speed optical downlink from orbiting communication satellites.

AO system design is application specific. For satellite-to-ground optical downlinks, the temporal bandwidth and strength of the wavefront deformations can be large due to poor seeing conditions at the receiver site (i.e., receiver sites may not be in favorable weather locations) which is further exacerbated by the fast movement of low earth orbit (LEO) satellites across the horizon. SatCom AO systems encounter wavefront fluctuations faster than 1 millisecond and with $\frac{D}{r_0} \geq 10$ [2]. Unfortunately, standard wavefront sensing using camera-based technologies, such as the Shack-Hartmann WFS, is challenging at the telecom wavelength of 1550nm due to the lack of affordable high speed, short-wave infrared (SWIR) image sensors. Image sensors operating in the mid-wave and long-wave infrared (MWIR, LWIR), which may be favored due to increased resilience to scattering as compared to SWIR [4], are even more limited in terms of speed and affordability. Thus, for optical SatCom applications, there is a strong need to develop WFS technologies that do not rely on cameras for detection.

In the standard modal wavefront sensing approach, a (e.g., Zernike) modal bias is applied to the incoming wavefront via a DM or a spatial light modulator (SLM) [5,6]. The resulting change in focal spot intensity is then recorded by one or more photodiodes. When there are only a few modes in the beam and their magnitudes are small, this approach works well due to the approximately linear relationship between the change in intensity and modal coefficient. However, this relationship is not valid in strong turbulence because of the number and magnitude of the modes present. That is, modal crosstalk precludes traditional modal wavefront sensing in turbulent optical SatCom downlinks.

Recently, more complex correction schemes have been introduced that permit modal wavefront sensing of turbulent wavefronts [7,8], through complex per-mode calibration. Even with this advancement, practical modal WFSs require a camera, or modal biases must be displayed sequentially via an SLM or a DM. The approximately millisecond settling time of these devices poses a significant limitation. For example, estimating 10 modes requires 20 measurements, necessitating at least 20ms of total settling time (<50Hz) – far too slow for atmospheric phase fluctuations [9,10].

Another recent development uses a photonic lantern to provide phase diversity to an input beam [11,12]. This intensity distribution at the output of the photonic lantern is used as input to a neural network (NN) that estimates the first 9 Zernike modes with high accuracy. However, this approach was demonstrated on input wavefronts containing only low-order modes, and using multiple photodiodes (or a camera). At present it is unclear how this approach could be scaled to realistic turbulence strengths.

Single-pixel imaging architectures have been explored as image sensor-less alternatives for WFS. These approaches typically employ a digital micromirror device (DMD) to modulate the incoming beam either at the pupil plane or at the focal plane. Pupil plane holograms provide a means to perform modal wavefront sensing [13], but suffer from very low efficiency (~1.5%), and require switching between each measured mode. In strong turbulence with many modes, this could easily reduce sensing speed to well below 1kHz. When the DMD is placed at the focal plane, the intensity of the focal plane can be probed directly. This has yielded promising results, with more efficient reconstruction algorithms currently in progress [14]. In this paper, we explore an alternative single-pixel architecture arrangement that also leverages the power of neural networks (NNs).

To circumvent the limitations of previous image sensor-less WFS sensing techniques, we pursue a modal wavefront sensing scheme that requires active modulation of only a single

aberration, and a single pixel photodetector (i.e., a photodiode). We show that modulation of the incoming beam with fast mirror technologies, such as a tip/tilt mirror (TTM) or defocus mirror, results in rapid intensity fluctuations that can be used to accurately estimate the phase distortion of the incoming laser beam via a NN. The NN is key to recovering the phase profile of wavefront ϕ from the measured intensity I due to their highly nonlinear relationship: $I \propto \exp(-i\phi)$.

We consider our technique a modal WFS approach because we train NNs to estimate modal coefficients of the incoming wavefront using a time-varying photodiode signal as input. In the special case of tip/tilt modulation in the pupil plane, this time-varying signal is the intensity of the focal plane along a curve prescribed by the tip/tilt trajectory. We show that even though the focal plane intensity is significantly undersampled, the wavefront can be accurately estimated to diffraction-limited accuracy. This is possible because the NN learns the statistics of the turbulence in the supplied training data, resulting in a strong prior that reduces the set of possible solutions to an intensity input.

Previous modal wavefront sensing schemes aim to minimize modal crosstalk by working in the linear regime where phase error is small [5,6]. This is severely limiting, even for moderate turbulence conditions, and prevents the use of such approaches to optical SatCom applications. Instead, our approach takes advantage of modal crosstalk to extract the amplitude of higher order modes, even those that are not modulated by the mirror (i.e., higher order than tip/tilt). Conveniently, the nonlinear relationship between phase and intensity couples all modes present in the input phase to the phase tip/tilt actively modulated by the TTM. We find similarly impressive results when simulating a rapidly oscillating defocus. In both cases, the NNs recover wavefront corrections for 50 modes of $D/r_0 = 10$ turbulent input beams with resulting Strehl ratios of 0.82. This is equivalent to 99% of the Strehl ratio of an optimally corrected 50-mode wavefront and is achieved at a sensing rate of 2 kHz (500 μ s of input data).

2. Simulation Setup

2.1 Optical setup

The simulated optical layout is shown in Fig. 1a. Consider a static aberrated beam entering the receiver aperture (diameter D) which is imaged via a 4f lens pair onto a TTM or DM. A subsequent lens, placed one focal length behind the TTM or DM, focuses light onto a pinhole detector. We assume that the TTM or DM is driven sinusoidally, thereby imparting a time varying phase deformation onto the reflected beam:

$$M_\phi(\mathbf{r}, t) = \sum_{k=1}^K a_k Z_k \sin(2\pi f_k t) \quad (1)$$

where a_k is a scalar amplitude of Zernike mode Z_k . We use the Noll ordering: $k = 2, 3$ specify x- and y- tilts and $k = 4$ is defocus. For a TTM, only a_2 and a_3 are non-zero while in the case of a DM, only a_4 is non-zero. The total phase profile $\phi(\mathbf{r}, t)$ of the incoming beam after reflection off the DM is given by:

$$\phi(\mathbf{r}, t) = \Phi(\mathbf{r}) + M_\phi(\mathbf{r}, t) \quad (2)$$

where $\Phi(\mathbf{r})$ is the phase profile of the incoming aberrated beam.

While $M_\phi(\mathbf{r}, t)$ could in principle take any functional form supported by a DM, we propose using either tip/tilt or defocus for phase diversity due to their ease of implementation. Widely available resonant galvo scanning and piezo-driven TTMs can operate in excess of 10kHz [15,16], while a DM could be used to modulate defocus at a few kHz [17,18]. In our approach, modulating higher order modes is unnecessary for turbulent wavefront

estimation, because the nonlinear relationship between intensity and phase couples all modes in the turbulent wavefront to the additional tip/tilt/defocus imparted by the active mirror.

The phase of an example turbulent wavefront, and the instantaneous tilt phase imparted by a TTM at time $t = \tau$ are shown in Figs. 1b and c, respectively. This time-varying tilt results in a dynamic displacement of the PSF at the detector plane. The effective scan trajectory of the detector on the PSF is shown in Fig. 1d, for $f_2 = 6\text{kHz}$; $f_3 = 4\text{kHz}$, both with amplitude 8π rad, forming a Lissajous pattern [19,20]. Other scan patterns are possible, however, Lissajous patterns are ideal for high-speed operation as they maximize the mechanical bandwidth of the TTM. The instantaneous detector position due to the tilt shown in Fig. 1c is denoted by the white spot in Fig. 1d.

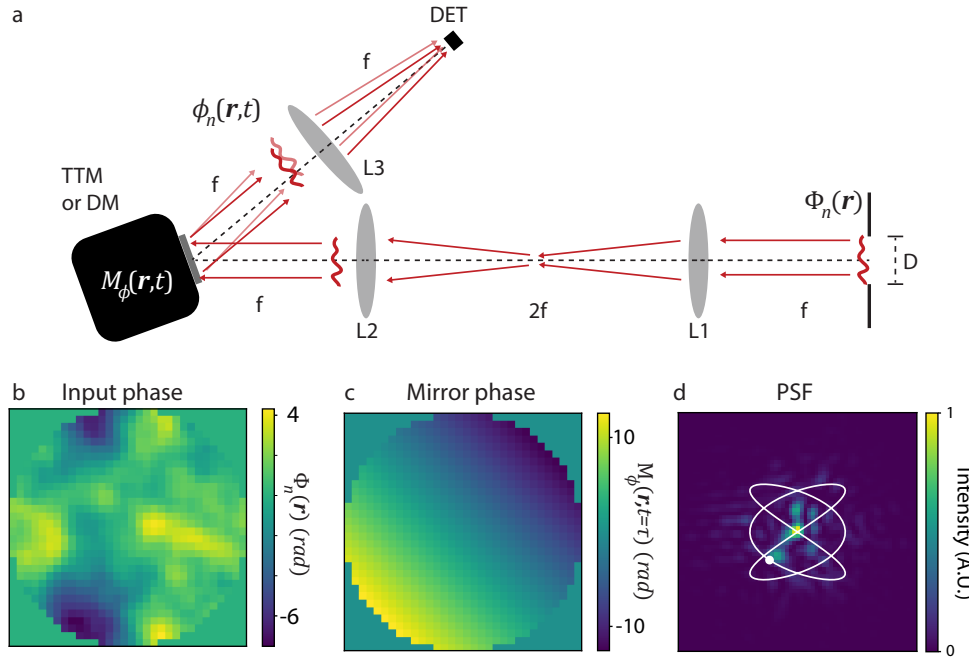


Fig. 1. a) Simulated optical setup in this work. The input phase arrives through an aperture of diameter D and is reimaged onto a tip-tilt mirror (TTM) or deformable mirror (DM) via a $4f$ system formed by lenses L1 and L2. The TTM or DM imparts an additional phase M_ϕ onto the incident wavefront (input) phase Φ_n to produce a total phase ϕ_n . For a TTM, M_ϕ is a linear phase ramp with sinusoidally varying amplitude; for a DM M_ϕ can be more complex. The Fourier transform of this mirror-modulated electric field is imaged onto a point detector (DET), via L3. b) Example input phase. c) Example instantaneous phase applied to the input phase via a TTM. d) PSF of the input phase. The effective detector position due to tilt in (b) is shown as a white spot. The white curve shows the Lissajous scan trajectory of the effective detector position in the PSF plane.

In addition to tip/tilt modulation, we also explore defocus modulation via a DM. For defocus modulation results below, we assume oscillation of the defocus aberration term of the DM at a frequency $f_4 = 2\text{kHz}$ with amplitude 8π rad with tip/tilt unmodulated.

2.2 Neural network training

We use the AOtools package [13] to create a training set of N independent static turbulent phase profiles $\Phi_n(\mathbf{r})$. Unless otherwise noted, we used the “ft_phase_screen” AOtools

function to create $N = 500,000$ training phase screens with modified Von Karman statistics, and 10% (50,000) of the training phase screens are reserved for validation (i.e., not used for training). The inner and outer scales are constant for all data in the paper: $l_0 = 5\text{cm}$; $L_0 = 15\text{m}$, respectively. The $\Phi_n(\mathbf{r})$ are sampled on a 32x32 pixel grid and are cropped to a circle of diameter 32 pixels to simulate input through the circular aperture of the receiver of diameter $D = 50\text{cm}$. For datasets with constant r_0 , we set $D/r_0 = 10$ (i.e. $r_0 = 5\text{cm}$); for datasets with variable D/r_0 , the D/r_0 range is stated explicitly. An example $\Phi_n(\mathbf{r})$ produced using these parameters (with $D/r_0 = 10$) is shown in Fig. 1b.

Training a NN to recover the input phase directly in the Cartesian basis is computationally intensive because it requires the NN to output a phase value for each pixel in the 32x32 grid. To reduce the dimensionality of the wavefront estimation problem, we seek to represent $\Phi_n(\mathbf{r})$ in a more compact modal basis. While the Zernike basis is often used in AO, the highly oscillatory behaviour of higher order Zernike modes near the periphery of the aperture make them problematic for numerical computation and physical creation on a DM [22,23]. Moreover, Zernike modes are not the most compact basis for turbulent wavefronts due to statistical correlations between Zernike coefficients. Instead, it is advantageous to use the Karhunen-Loeve (KL) basis, wherein the modal coefficients are statistically uncorrelated [24–26]. For a finite number of modes, the KL representation of a turbulent phase screen is more accurate than the Zernike representation. For these reasons, we decompose the $\Phi_n(\mathbf{r})$ into a numerical approximation of the KL basis: the principal components. We calculate the first M principal components using the principal components analysis (PCA) class in the Python module scikit-learn:

$$\Phi_n(\mathbf{r}) \approx \sum_{m=0}^M a_{nm} P_m(\mathbf{r}) \quad (3)$$

where a_{nm} is the coefficient of the principal component $P_m(\mathbf{r})$ in $\Phi_n(\mathbf{r})$. We will call the principal components the “PCA modes” to align with the nomenclature of Zernike modes. In Fig. 2a-b, we show a comparison between PCA modes and Zernike modes. The two modal sets look similar for low mode numbers but then diverge as mode number increases.

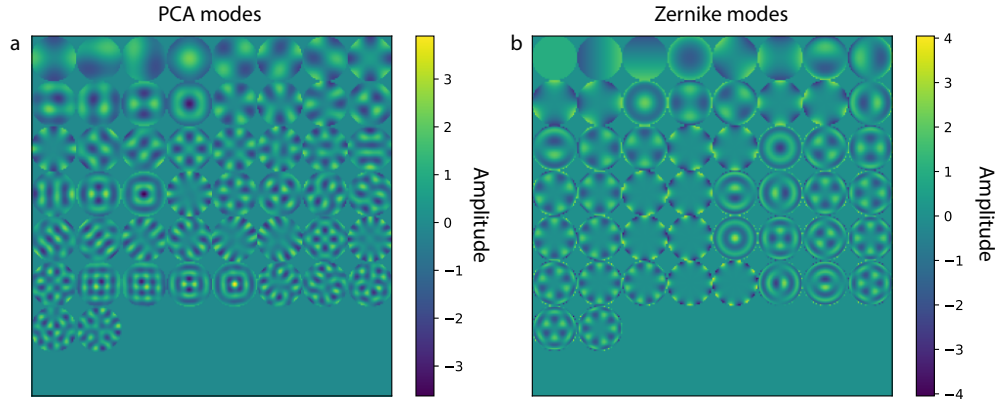


Fig. 2. a) The first $M=50$ PCA modes for turbulent phase screens. b) First 50 Zernike modes.

The intensity at the pinhole detector $I_n((0,0), t)$ is assumed to be proportional to the Strehl ratio (i.e., the on-axis intensity). We calculate the Strehl ratio S as

$$I_n((0,0), t) \propto S_n(t) = |\langle \exp(-i\phi_n(\mathbf{r}, t)) \rangle_r|^2 \quad (4)$$

Where $\langle \cdot \rangle_r$ denotes a spatial average taken over the DM aperture and $\phi_n(\mathbf{r}, t) = \Phi_n(\mathbf{r}) + M_\phi(\mathbf{r}, t)$ is the time varying phase error (piston-removed) over the DM aperture. This intensity signal is sampled at 250kHz. This sampling rate was chosen to match the maximum sampling rate of a low-cost USB A/D converter (National Instruments USB-6210), in anticipation of future experimental implementation. Note that ϕ_n varies in time due to the continuous driving of the TTM/DM, not due to any change in the static incoming aberrated beam. We simulate the acquisition of 125 such timepoints over a 500 μ s time window. We assume that the phase distortion $\Phi_n(\mathbf{r})$ is static over the measurement period

When assessing the robustness of our technique to noise, we incorporate photon shot noise in the following way. The number of detected photons per sample (N_p) is set for a Strehl ratio of 1, and then Poisson noise is added to the measurement with variance and mean value determined by the noiseless signal. We denote the resulting noisy intensity trace by $\tilde{S}_n(t)$. An example noisy intensity trace for the phase screen and scan trajectory in Figs. 1b,d is shown in Fig. 3a, with a Strehl ratio of 1 corresponding to $N_p = 10^7$ detected photons/sample. At 1550nm, this corresponds to a maximum detected power of 320nW. Note that at this power level, Poisson noise is not apparent on the scale of the plot in Fig. 3a.

The training set consists of pairs of $S_n(t)$ and $\Phi_n(\mathbf{r})$. Our goal is to train a NN to accept $S_n(t)$ in Eq.4 as input, and output an estimate the coefficients a_{nm} that describe $\Phi_n(\mathbf{r})$ as in Eq.3. Working in the PCA basis reduces the dimensionality of the problem to finding M scalar values instead of attempting to recover the phase at every pixel within a diameter of 32 pixels (total 805 pixels). Here we choose $M = 50$ PCA modes as a compromise between high fidelity wavefront reconstruction and network size. Note that additional modes can be incorporated at the expense of greater NN complexity.

We initially trained a single NN with 3 fully connected hidden layers with 1024 nodes to estimate the first $M = 50$ PCA modes from an input intensity trace, using Tensorflow [27]. After each fully connected layer, a dropout ratio of 0.01 was applied to prevent overfitting. More details on the NN architecture and training parameters can be found in Tables 1 and 2. When attempting to train a single NN estimate with $M = 50$ modes, we found large errors in the higher order PCA mode coefficients, approaching 100% of the mean coefficient magnitude for PCA mode 50 (ie. mean error \approx mean magnitude). We hypothesized that this occurs due to the mean-squared-error loss function used in NN training biases training towards fitting the modes with the largest magnitude. For turbulent wavefronts, modal coefficients are typically largest for the lowest order modes. Standard NN training is unable to adjust the network to accommodate such disparate average magnitudes in modal coefficients.

We attempted to alleviate this issue by normalizing the magnitude of the PCA mode coefficients by their variance during training. This resulted in uniform, but poor, accuracy for all $M = 50$ modes. Instead, we found it advantageous to train 10 NNs each outputting a group of 5 of PCA mode coefficients. Larger or smaller mode groupings may also be chosen. This approach reduces the range of variance of the modes that are considered by each NN. For example, NN_a estimates mode coefficients for PCA modes 0-4; NN_b coefficients for PCA modes 5-9, and so on up to PCA mode 50. The resulting PCA mode coefficient estimates are then concatenated into a 50-element PCA mode coefficient vector. The 2D representation of the wavefront estimate is obtained by matrix multiplication of the PCA mode coefficient vector by the PCA mode matrix (Eq. 3).

Table 1. Neural network parameters

Network parameter	Value
Input vector size	1x125
Output vector size	1x5
# of networks	10 (5 modes/network, total 50 modes)

# hidden layers / network	3 (fully connected)
Layer activation	ReLU
# Nodes/layer	1024
Dropout ratio	0.01
Inference time	<3ms/10 NNs (total 50 modes)

Table 2. Neural network training parameters

Training property	Value
Loss function	Mean-squared error
Optimizer	ADAM
Epochs	320
Learn rate	0.00005 (epochs 1-150), 0.00005 (epochs 151-300), 0.00001 (epochs 301-320)
Batch size	1000
Training set	450,000 pairs of $S_n(t)$ and $\Phi_n(\mathbf{r})$
Validation set	50,000 pairs of $S_n(t)$ and $\Phi_n(\mathbf{r})$
Total training time	~3 hrs on Nvidia 3060Ti GPU

3. Results

To estimate the wavefront, the input intensity trace is run through each network and the output mode coefficients are concatenated and then multiplied by their respective PCA modes (Fig. 2a) and summed. An example wavefront estimation is shown in Fig. 3 for tip/tilt modulation. The time trace in Fig. 3a, produced by the turbulent phase in the inset, is passed through the NNs. The first 25 NN-estimated PCA mode coefficients are shown in Fig. 3b, along with the resulting estimated wavefront (using 50 PCA modes) in the inset. Qualitatively, there is good agreement between the ground truth and estimated PCA mode coefficients and wavefronts. Note that the estimated wavefront in the inset of Fig. 3b resembles a smoothed version of the ground truth (Fig. 3a inset) due to the truncation at 50 modes.

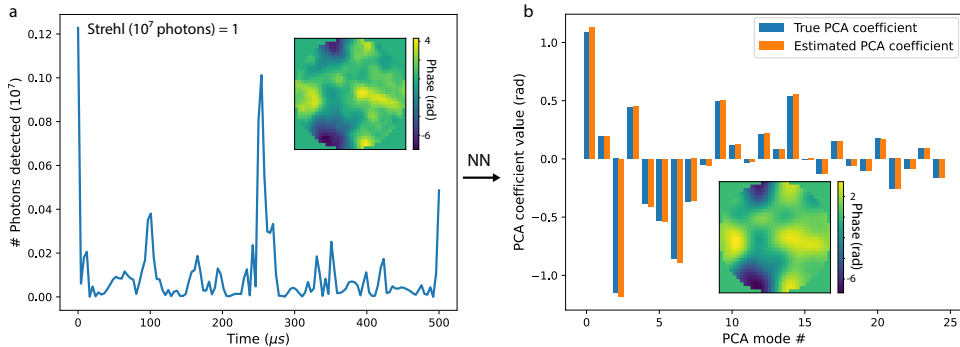


Fig. 3. a) Example simulated intensity time trace. This is used as input to the trained NN to estimate PCA mode coefficients. Inset shows the input phase across the receiver aperture. This is the same phase screen as shown in Fig. 1b, and the intensity trace is obtained by plotting the intensity along the trajectory shown in Fig. 1d. b) True (blue) and estimated (orange) values of

the PCA coefficients for the turbulent input phase used to simulate the intensity time trace in (a). The inset shows the NN estimate of the input phase.

To quantify the accuracy of this technique, we calculate the root-mean-squared (RMS) error between the true and NN-estimated PCA coefficients as

$$\text{RMS error} = \sqrt{\frac{1}{N_v} \sum_n |a_{nm,NN} - a_{nm}|^2} \quad (4)$$

Where $a_{nm,NN}$ and a_{nm} are respectively the NN-estimated and ground truth mode coefficient values for mode m of phase screen n and $N_v = 50000$ indicates the number of validation turbulent wavefronts not used for training. The result is shown in Figs. 4a,c for both tip/tilt and defocus modulation schemes, respectively. RMS error decreases rapidly with mode number because higher PCA modes (which have high spatial frequencies) contribute less to the input phase according to the turbulence statistics. This is the same effect that contributes to poor performance when training a single NN for all modes, as discussed in the previous section. This effect can also be seen as a rise in mean relative error with increasing mode number, as shown in Figs. 4b,d. Here, the mean relative error is the mean absolute error divided by the mean PCA coefficient magnitude, i.e.,

$$\text{Mean relative error} = 100\% \times \left(\frac{1}{N_v} \sum_n |a_{nm,NN} - a_{nm}| \right) / \left(\frac{1}{N_v} \sum_n |a_{nm}| \right) \quad (5)$$

The estimation of higher order PCA modes is more error prone due to their diminishing prevalence in the turbulence spectrum, and therefore have a reduced effect on the loss function during NN training. Although this is mitigated by training multiple NNs, we still see increasing relative error within each group of 5 modes estimated by a single NN (indicated by gray and white regions in Figs. 4b,d).

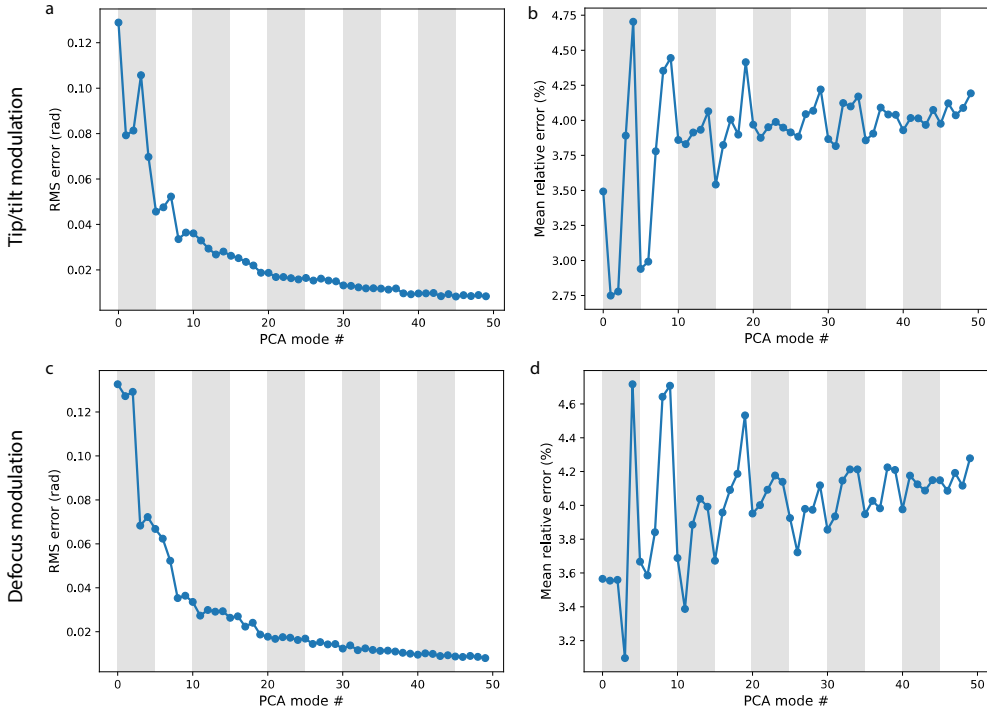


Fig. 4. a) RMS error between true and NN-estimated PCA mode coefficients as a function of PCA mode #, for tip/tilt modulated training data. The RMS error is calculated over 50000 validation pairs of intensity traces and input phase screens. b) Mean relative error between true and NN-estimated PCA coefficients expressed in %. Alternating gray and white backgrounds show the border between each 5-mode NN. c) and d) are the same as a) and b), but for defocus modulated training data.

The total mean RMS error of the NN-estimated wavefront, including modes not estimated by the NNs, and averaged over all validation phase screens, is 0.46 rad (Figs. 5a,c) for both tip/tilt and defocus modulation. We compare this with the total RMS error histogram for the input wavefront and the optimal 50-mode correction, where the RMS errors (labeled RMSE in Fig. 5 and below) are defined as follows

$$\text{RMSE}_{\text{in}} = \sqrt{\frac{\iint_{\text{aperture}} |\Phi_n(r)|^2 dr}{A}} \quad (6)$$

$$\text{RMSE}_{\text{opt}} = \sqrt{\frac{\left(\iint_{\text{aperture}} |\Phi_n(r)|^2 dr - \sum_{m=0}^{49} a_{nm} P_m(r) \right)}{A}} \quad (7)$$

$$\text{RMSE}_{\text{NN}} = \sqrt{\frac{\left(\iint_{\text{aperture}} |\Phi_n(r)|^2 dr - \sum_{m=0}^{49} a_{nm,NN} P_m(r) \right)}{A}} \quad (8)$$

Where A is the area of the input aperture. In practice, we approximate the integrals in Eqs.6-8 by discrete sums over the pixels representing the circular aperture. The histogram of total wavefront RMS error achieved with NN estimation (RMSE_{NN} , green histograms in Figs. 5a,c)

overlaps almost completely with the optimal 50-mode correction (RMSE_{opt} , orange histograms in Figs. 5a,c), indicating high quality wavefront estimation.

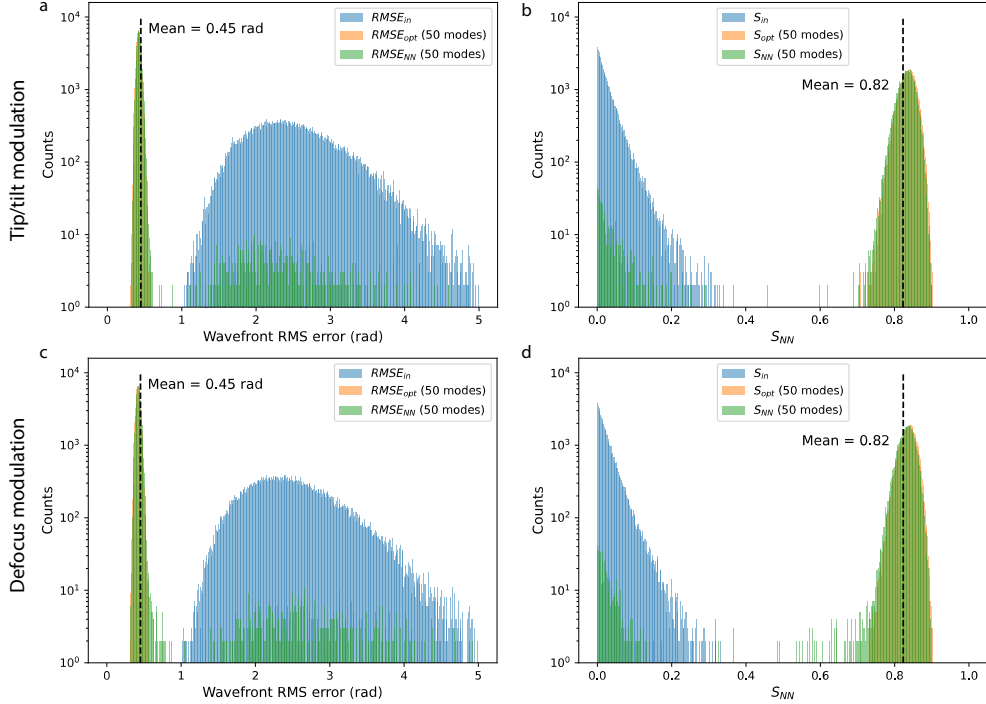


Fig. 5. a) Histograms of the wavefront RMSE of input phase (RMSE_{in}), the optimally corrected phase (RMSE_{opt}), and the corrected phase based on the estimate of the NN (RMSE_{NN}), using tip/tilt modulated training data. The optimally corrected phase indicates a perfect correction for the first 50 PCA modes. b) As in (a), but for the resulting Strehl ratio (S). In both cases, the histograms resulting from NN estimate are almost entirely overlapping with histograms resulting of optimal 50 PCA mode correction. c) and d) are the same as (a) but for defocus modulated training data.

In practice for space to ground telecom applications, we are not directly concerned with wavefront RMS error, but rather with the intensity coupled into a single mode optical fibre (SMF). For simplicity, we use the Strehl ratio (proportional to the on-axis focal spot intensity) as a proxy for the power coupled into a SMF, though in reality modal overlap must be considered. The Strehl ratio of a simulated AO-corrected wavefront using NN and optimal 50-mode corrections is calculated as

$$S_{NN,n} = \left| \left\langle \exp \left(-i(\Phi_n(\mathbf{r}) - \sum_{m=0}^{49} a_{nm,NN} P_m(\mathbf{r})) \right) \right\rangle_r \right|^2 \quad (9)$$

$$S_{opt,n} = \left| \left\langle \exp \left(-i(\Phi_n(\mathbf{r}) - \sum_{m=0}^{49} a_{nm} P_m(\mathbf{r})) \right) \right\rangle_r \right|^2 \quad (10)$$

$S_{NN,n}$ and $S_{opt,n}$ are the on-axis intensity at the detector due to an open-loop AO correction of Φ_n using NN-estimated or ground truth (optimal) modal coefficients. On average, the Strehl ratio of the NN-estimated correction is 0.82 (Fig. 5b,d) for both tip/tilt and defocus modulation, exceeding the rule of thumb Rayleigh criterion (0.8) for a diffraction-limited focus quality. A larger number of sensed modes will lead to a further improved Strehl ratio but will only be useful if the correcting DM has enough actuators to apply the correction.

3.1 Generalizability

To test the efficacy of our technique across a more general range of conditions, we benchmarked the average Strehl ratio for the corrected wavefront $\langle S_{NN} \rangle$ against that of the optimal 50-mode correction $\langle S_{opt} \rangle$ and the average input Strehl ratio $\langle S_{in} \rangle$, as a function of D/r_0 value. Figures 6a-b show that for increasing D/r_0 values, both $\langle S_{in} \rangle$ and $\langle S_{opt} \rangle$ decrease, as expected. $\langle S_{NN} \rangle$ peaks for the turbulence strength used in training ($D/r_0 = 10$) and then drops off on either side. Interestingly, NNs trained on tip/tilt modulated data generalized slightly better to other turbulence strengths than those trained on defocus modulation data, as evidenced by the widths of the peaks of the green curves in Figs. 6a-b and Fig. 7. At this peak performance, the correction efficacy $\langle S_{NN}/S_{opt} \rangle$ of the tip/tilt trained NNs reaches a value of 0.99 (Fig. 7, purple), indicating a nearly optimal Strehl ratio for a 50-mode correction: only 1% more light could be directed to the focus for a 50-mode correction. The defocus trained NNs reach nearly the same accuracy, with peak $\langle S_{NN}/S_{opt} \rangle \approx 0.98$.

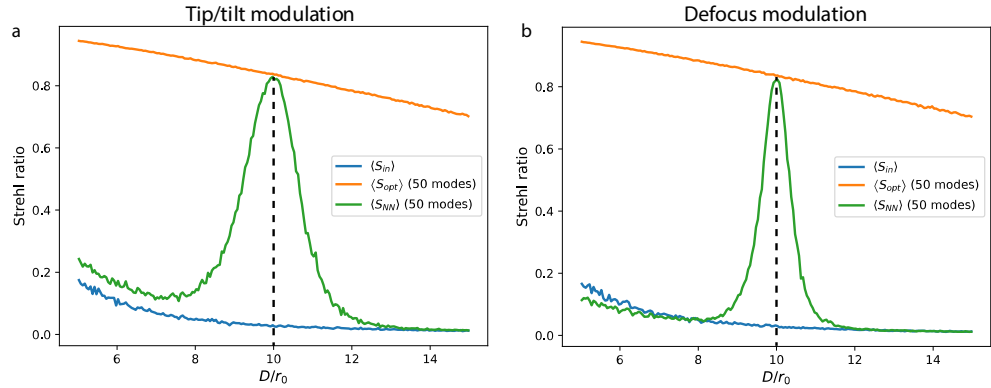


Fig. 6. a) Performance of a NN trained on tip/tilt modulation with $D/r_0 = 10$ data when using $D/r_0 = 5 - 15$. $\langle S_{NN} \rangle$ is highest when the input intensity trace results from phase screens with $D/r_0 = 10$, and falls to $\langle S_{NN} \rangle \approx \langle S_{in} \rangle$ for $D/r_0 < 8$, $D/r_0 > 12$. b) As in (a), but for defocus modulation.

Evidently, the NNs need to be trained for the correct D/r_0 for accurate results. In practice, one may employ several groups of NNs, each trained on a different D/r_0 values. The input data could then be fed into the appropriate NN with knowledge of the current seeing conditions. Alternatively, NNs trained on a more general training set may be employed.

We explored the generalizability of NNs trained on multiple D/r_0 values for tip/tilt modulation. When training with a dataset composed of equal numbers of $D/r_0 = 9, 11$ phase screens (green curve, Fig. 7), we observe two corresponding peaks where $\langle S_{NN}/S_{opt} \rangle \approx 0.91$. We suspect that the diminished correction accuracy is due to a dilution of training data: only half of the training set is available at each D/r_0 value.

Next, we investigated training NNs with a uniform D/r_0 distribution from 5 – 15, again with tip/tilt modulation. We found that increasing the amount of training data from 500k to 2M training pairs improved NN performance significantly; the resulting correction efficacy is shown in the black curve in Fig. 7. Although the maximum value of $\langle S_{NN}/S_{opt} \rangle \approx 0.77$, is lower than for NNs trained on only one or two discrete D/r_0 values, it is relatively flat over $D/r_0 \approx 6 - 14$, which may be a significant advantage in evolving turbulence conditions.

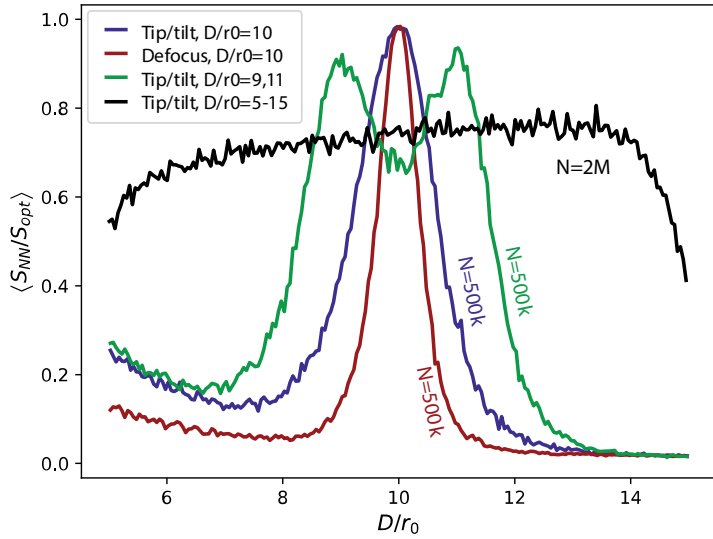


Fig. 7. b) $\langle S_{NN}/S_{opt} \rangle$ as a function of D/r_0 for different training datasets. The D/r_0 indicated in the legend is the range of D/r_0 in the training dataset. The phase modulation scheme used to generate training data is noted in the legend (tip/tilt or defocus modulation).

In addition to the generalization of NNs to variable turbulence strength, we also investigated their generalizability to different turbulence statistics. We considered two common turbulence models: modified Von Karman and Kolmogorov. Kolmogorov phase screens have a spatial frequency spectrum which decays as $k^{-11/3}$ as compared to $k^{-11/6}$ for Von Karman [28]. We found that estimating a Kolmogorov phase screen using NNs trained on Von Karman statistics yielded no improvement over the input phase screen's Strehl ratio (Fig. 8a). This indicates that the underlying statistics of the phase screen distribution is a critical prior that enables NNs to perform accurate phase screen estimation.

Instead of training NNs on only modified Von Karman statistics (as in all previous results presented in this paper), we generated a dataset composed of 500k Von Karman phase screens and 500k Kolmogorov phase screens, all with $D/r_0 = 10$. We then trained NNs with this combined training set (using TTM modulation) and found that we recovered nearly optimal phase screen estimation accuracy, as shown in Figs. 8b,c. The difference in the Strehl ratios between Von Karman and Kolmogorov datasets stems from the different input wavefront statistics of the two statistical models. Most importantly, the NN-estimated (green) histograms overlap nearly completely with that of the optimal 50-mode estimates (orange) in Fig. 8b,c, just as in Figs. 5a-b. Validation performance for both statistical models is identical when benchmarked against the optimal 50-mode phase screen estimate (Figs. 8a-b vs. Figs. 8c-d), with $\langle S_{NN}/S_{opt} \rangle = 0.98$ in both cases. Interestingly, the Strehl ratios of the optimal 50-mode corrections for Kolmogorov input wavefronts are lower when using the Von Karman trained NNs (orange histogram in Fig. 8a) compared to the Von Karman + Kolmogorov NNs (orange histogram in Fig. 8b). This is because the PCA mode basis differs between the two training sets as can be seen by comparing Figs. 2a and 8d. This indicates that the selection of the PCA mode basis plays an important role in the performance of our technique by providing a basis that allows for optimal correction of a small number of modes, and is specific to the turbulence statistics.

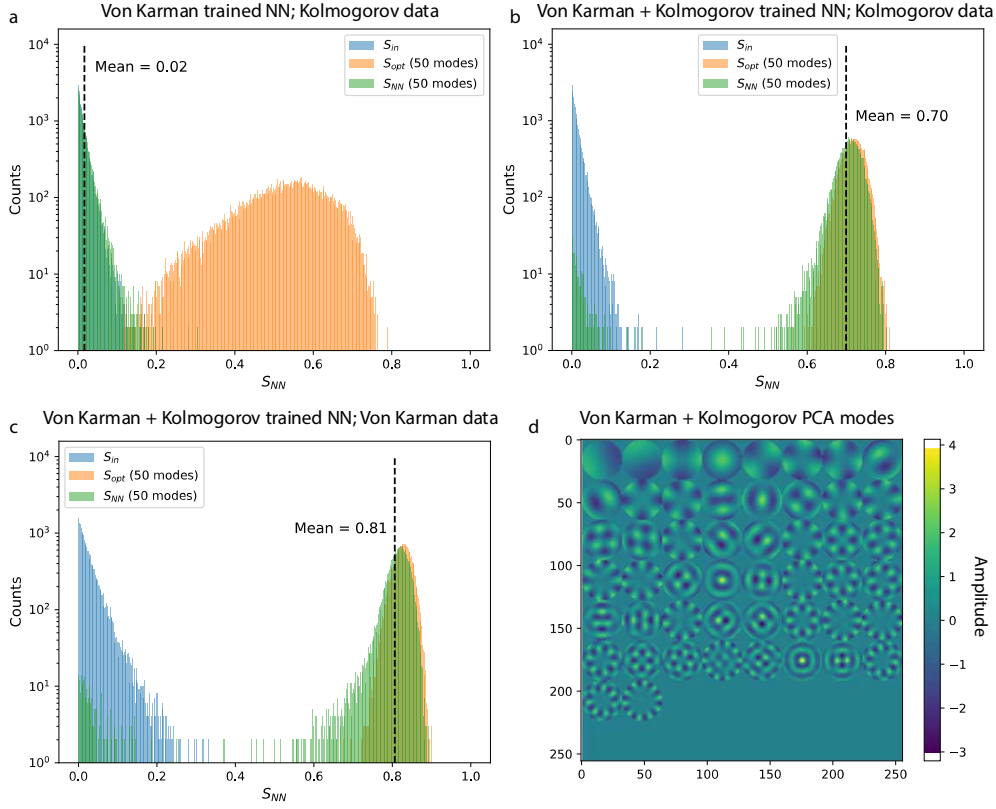


Fig. 8. a) Strehl ratio histograms for input, optimal, and NN-estimated Kolmogorov wavefronts using Von Karman-trained NNs. b) As in (a), but with NNs trained on a combination of Von Karman and Kolmogorov data. c) As in (b) but for Von Karman validation data. Wavefront estimation performance is nearly identical to Von-Karman-only trained NNs (see Fig. 5b). d) PCA modes for the combined Von Karman and Kolmogorov training set (compare to Fig. 2a).

3.2 Performance with noisy data

The results presented thus far were achieved with an input intensity signal with a large detected optical power. We investigated the effect of increasing Poisson noise by estimating turbulent wavefronts from Poisson-noise corrupted intensity traces $\tilde{S}_n(t)$, with $\langle S_{NN}/S_{opt} \rangle$ as the performance metric. Typical received beam powers for space to ground downlink are expected to be in the range of 100s – 1000s of nW at 1550nm [29]. Ideally, only a small fraction of this received optical power is consumed for wavefront sensing. We find that for max focal spot powers $> 1\text{nW}$ at 1550nm, the performance saturates at $\langle S_{NN}/S_{opt} \rangle \approx 0.99$ (Fig. 9). Here, the max focal spot power is the detected optical power for Strehl ratio = 1, the integration time is 500 μs , and tip/tilt modulation is used. Sensing performance is still good at 0.15nW, with $\langle S_{NN}/S_{opt} \rangle \approx 0.8$. In terms of actual detected photon numbers, this power level corresponds to an average of 40 photons detected per time sample, or 5000 total detected photons. At 0.032nW, the average number of detected photons per time sample drops to 8.5, yet the NNs still achieve modest performance, with $\langle S_{NN}/S_{opt} \rangle \approx 0.37$. Interestingly, we found that fine tuning or training NNs with noisy instead of noiseless data yielded worse results. This indicates that performance on noisy data may be improved by preprocessing intensity traces to smooth out noise, however, this is beyond the scope of this work.

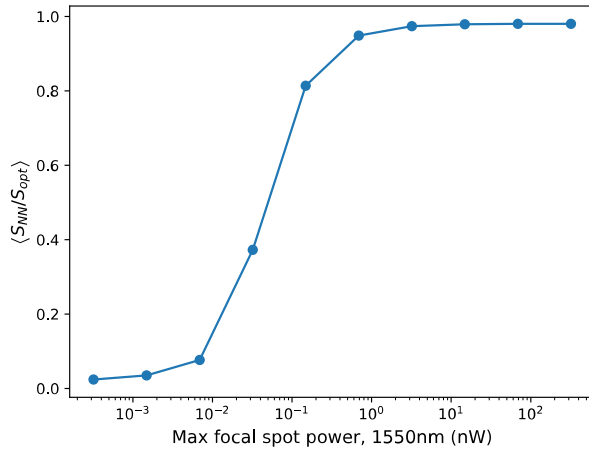


Fig. 9. Performance of NN wavefront sensing in the presence of Poisson noise. Here the amount of Poisson noise is prescribed via the max focal spot power (power of focal spot when Strehl ratio = 1) at 1550nm. Figures, supplementary materials, and tables

4. Conclusions

In this work we presented a novel single-pixel wavefront sensing architecture. Our technique uses a single photodetector, making it more cost effective and applicable in the SWIR where it is challenging to find cameras to power wavefront sensors at >kHz rates [30,31]. Moreover, the use of a TTM or a focusing DM lends itself to robust implementation using off-the-shelf components.

The approach presented in this paper can be directly applied to realize a wavefront sensor to drive a traditional AO system. Alternatively, it can also be integrated with the system's main detector and DM. In the latter configuration, an initial modulation of the TTM/DM and subsequent NN estimation of the turbulent wavefront would lead to a corrected wavefront and a closed AO loop. Once the AO loop is closed, a small DM modulation can be applied and the resulting intensity trace used as input to an NN to estimate the dynamic turbulent wavefront evolution. If the TTM/DM modulation is small enough, it is anticipated that the resulting focal spot intensity variation will also be small, avoiding significant impact the quality of the received data via fading, for example, in telecom applications.

The integration of our NN technique into an AO correction loop will require real-time low latency inference with the trained NNs. A full inference (estimation) of 50 modes using 10 NNs takes <3ms total on our 3060Ti GPU. This is still approximately an order of magnitude larger than the 2-4 kHz acquisition rate proposed in this paper. Achieving AO loop implementation at the >kHz rates enabled by our approach will require optimization of the NNs and faster GPUs. While such a development is beyond the scope of this work, we note that NN weight quantization and dynamic range tuning approaches have been shown as a straightforward approach to gain a two times speed up in inference with minimal accuracy loss [32].

In future work, we plan to experimentally validate the simulations presented in this paper using a spatial light modulator to physically simulate turbulent wavefronts. In particular, we will explore ways to maximize the acquisition rate of this technique. These results indicate that both tip/tilt scanning and defocus modulation variants are able to infer high accuracy phase screen estimates at an acquisition rates of 2kHz. Using readily available TTMs with resonant frequencies of 8, 12 kHz [16], the acquisition rate (inverse of the scan period of a complete Lissajous pattern) could be doubled to 4kHz. Alternatively, an axially scanning mirror placed

at the intermediate focus of the 4f system in Fig. 1a (above the ‘2f’) could also be used to implement defocus modulation. This arrangement has the advantage that a standard flat mirror could be driven back and forth at \sim 10-20kHz by a speaker coil, increasing the potential acquisition rate by an order of magnitude.

It is anticipated that such high-speed AO approaches are key in enabling terabit per second and beyond optical downlinks from LEO satellite constellations.

Funding. National Research Council of Canada - AI for Design project 136.

Acknowledgments. The authors would like to thank Jean-Pierre Veran, Maaike Van Kooten, Uriel Conod and Glen Herriot for stimulating discussion.

Disclosures. -

Data availability. Data underlying the results presented in this paper are not publicly available at this time but may be obtained from the authors upon reasonable request.

References

1. D. Giggenbach, "Deriving an estimate for the Fried parameter in mobile optical transmission scenarios," *Appl. Opt., AO* **50**, 222–226 (2011).
2. D. Giggenbach, F. Moll, and N. Perlot, "Optical Communication Experiments at DLR," *Journal of the National Institute of Information and Communications Technology* **59**, 125–134 (2012).
3. N. Devkota, N. Maharjan, and B. W. Kim, "Atmospheric Effects on Downlink Channel of Satellite to Ground Free Space Optical Communications," in *2022 13th International Conference on Information and Communication Technology Convergence (ICTC)* (2022), pp. 1335–1340.
4. L. Flannigan, L. Yoell, and C. Xu, "Mid-wave and long-wave infrared transmitters and detectors for optical satellite communications—a review," *J. Opt.* **24**, 043002 (2022).
5. M. A. A. Neil, M. J. Booth, and T. Wilson, "New modal wave-front sensor: a theoretical analysis," *J. Opt. Soc. Am. A, JOSAA* **17**, 1098–1107 (2000).
6. M. a. A. Neil, M. J. Booth, and T. Wilson, "Closed-loop aberration correction by use of a modal Zernike wave-front sensor," *Opt. Lett.*, **OL 25**, 1083–1085 (2000).
7. A. Zepp, S. Gladysz, K. Stein, and W. Osten, "Simulation-based design optimization of the holographic wavefront sensor in closed-loop adaptive optics," *Light: AM* **3**, 384–399 (2022).
8. A. Zepp, S. Gladysz, K. Stein, and W. Osten, "Optimization of the holographic wavefront sensor for open-loop adaptive optics under realistic turbulence. Part I: simulations," *Appl. Opt., AO* **60**, F88–F98 (2021).
9. L. C. Roberts, S. R. Meeker, J. Tesch, J. C. Shelton, J. E. Roberts, S. F. Fregoso, T. Troung, M. Peng, K. Matthews, H. Herzog, and J. Rodriguez, "Performance of the adaptive optics system for Laser Communications Relay Demonstration's Ground Station 1," *Appl. Opt., AO* **62**, G26–G36 (2023).
10. L. C. R. Jr, G. Block, S. Fregoso, H. Herzog, S. R. Meeker, J. E. Roberts, J. Rodriguez, J. Tesch, and T. Truong, "A laser communication adaptive optics system as a testbed for extreme adaptive optics," in *Adaptive Optics Systems VI* (SPIE, 2018), Vol. 10703, pp. 550–558.
11. J. Lin, M. P. Fitzgerald, Y. Xin, O. Guyon, S. Leon-Saval, B. Norris, and N. Jovanovic, "Focal-plane wavefront sensing with photonic lanterns: theoretical framework," *J. Opt. Soc. Am. B, JOSAB* **39**, 2643–2656 (2022).
12. B. R. M. Norris, J. Wei, C. H. Betters, S. G. Leon-Saval, Y. Xin, J. Lin, Y. J. Kim, S. Sallum, J. Lozi, S. Vieuard, O. Guyon, P. Gatkine, N. Jovanovic, D. Mawet, and M. P. Fitzgerald, "Demonstration of a photonic-lantern focal-plane wavefront sensor using fiber mode conversion and deep learning," in *Adaptive Optics Systems VIII* (SPIE, 2022), Vol. 12185, pp. 968–973.
13. M. A. Cox, E. Toninelli, L. Cheng, M. J. Padgett, and A. Forbes, "A High-Speed, Wavelength Invariant, Single-Pixel Wavefront Sensor With a Digital Micromirror Device," *IEEE Access* **7**, 85860–85866 (2019).
14. M. Pashazanoosi, M. Taylor, O. Pitts, C. Flueraru, A. Orth, and S. Hranilovic, "Maximizing atmospheric-disturbed fiber coupling efficiency with speckle-based phase retrieval and a single-pixel camera," *Appl. Opt., AO* **62**, G43–G52 (2023).

15. "S-331 High-Speed Tip/Tilt Platform," <https://www.pi-usa.us/en/products/fast-steering-mirrors-fsm-and-piezo-tilt-tilt-platforms-for-active-optics/s-331-high-speed-tilt-tilt-platform-300705>.
16. "Galvo-Resonant Scanners and Controllers," <https://www.thorlabs.com>.
17. "Deformable Mirrors for Wavefront Control," Boston Micromachines Corp (n.d.).
18. "Revibro Optics | Tunable Focus Mirror," <https://www.revibrooptics.com/products>.
19. D. Y. Kim, K. Hwang, J. Ahn, Y.-H. Seo, J.-B. Kim, S. Lee, J.-H. Yoon, E. Kong, Y. Jeong, S. Jon, P. Kim, and K.-H. Jeong, "Lissajous Scanning Two-photon Endomicroscope for In vivo Tissue Imaging," *Sci Rep* **9**, 3560 (2019).
20. J. Wang, G. Zhang, and Z. You, "Design rules for dense and rapid Lissajous scanning," *Microsyst Nanoeng* **6**, 1–7 (2020).
21. M. J. Townson, O. J. D. Farley, G. O. de Xivry, J. Osborn, and A. P. Reeves, "AOtools: a Python package for adaptive optics modelling and analysis," *Opt. Express, OE* **27**, 31316–31329 (2019).
22. V. Lakshminarayanan and A. Fleck, "Zernike polynomials: a guide," *Journal of Modern Optics* **58**, 545–561 (2011).
23. G. A. Papakostas, Y. S. Boutalis, C. N. Papaodysseus, and D. K. Fragoulis, "Numerical stability of fast computation algorithms of Zernike moments," *Applied Mathematics and Computation* **195**, 326–345 (2008).
24. R. J. Noll, "Zernike polynomials and atmospheric turbulence*," *J. Opt. Soc. Am., JOSA* **66**, 207–211 (1976).
25. G. Dai, "Modal wave-front reconstruction with Zernike polynomials and Karhunen–Loève functions," *J. Opt. Soc. Am. A, JOSAA* **13**, 1218–1225 (1996).
26. G. B. Scharmer, P. M. Dettori, M. G. Lofdahl, and M. Shand, "Adaptive optics system for the new Swedish solar telescope," in *Innovative Telescopes and Instrumentation for Solar Astrophysics* (SPIE, 2003), Vol. 4853, pp. 370–380.
27. "TensorFlow," <https://www.tensorflow.org/>.
28. P. Jia, D. Cai, D. Wang, and A. Basden, "Simulation of atmospheric turbulence phase screen for large telescope and optical interferometer," *Monthly Notices of the Royal Astronomical Society* **447**, 3467–3474 (2015).
29. M. W. Wright, J. F. Morris, J. M. Kovalik, K. S. Andrews, M. J. Abrahamson, and A. Biswas, "Adaptive optics correction into single mode fiber for a low Earth orbiting space to ground optical communication link using the OPALS downlink," *Opt. Express, OE* **23**, 33705–33712 (2015).
30. "HASO4 SWIR 1550 I Cost efficient wavefront sensor for 1.5-1.6um," Axiom Optics (n.d.).
31. "C-RED 2 | High-Speed Cooled SWIR camera," Axiom Optics (n.d.).
32. "Post-training quantization | TensorFlow Lite," https://www.tensorflow.org/lite/performance/post_training_quantization.